Folding of the C-terminal bacterial binding domain in statherin upon adsorption onto hydroxyapatite crystals

Gil Goobes[†], Rivka Goobes[‡], Ora Schueler-Furman[§¶], David Baker[§], Patrick S. Stayton[‡‖], and Gary P. Drobny[†‖]

Departments of [†]Chemistry, [‡]Bioengineering, and [§]Biochemistry, University of Washington, Seattle, WA 98195

Edited by Adriaan Bax, National Institutes of Health, Bethesda, MD, and approved September 14, 2006 (received for review August 18, 2006)

Statherin is an enamel pellicle protein that inhibits hydroxyapatite (HAP) nucleation and growth, lubricates the enamel surface, and is recognized by oral bacteria in periodontal diseases. We report here from solid-state NMR measurements that the protein's C-terminal region folds into an α-helix upon adsorption to HAP crystals. This region contains the binding sites for bacterial fimbriae that mediate bacterial cell adhesion to the surface of the tooth. The helical segment is shown through long-range distance measurements to fold back onto the intermediate region (residues Y16–P28) defining the global fold of the protein. Statherin, previously shown to be unstructured in solution, undergoes conformation selection on its substrate mineral surface. This surface-induced folding of statherin can be related to its functionality in inhibiting HAP crystal growth and can explain how oral pathogens selectively recognize HAP-bound statherin.

protein | solid-state NMR | structure | biomineralization | surface

Tooth enamel structural integrity is maintained through the supersaturation of saliva with respect to calcium and phosphate salts and the lubricative action of proteins in the pellicle coating the oral surfaces (1–5). Statherin and the proline-rich proteins (PRPs) prevent formation of accretions on the tooth surface by inhibiting both spontaneous calcium phosphate precipitation and hydroxyapatite (HAP) secondary crystal growth (6, 7). Statherin readily binds calcium ions in solution and adsorbs to HAP surfaces with a significant binding affinity and coverage (8–10). The proximity of statherin side chains to the surface and the mechanism of adsorption to HAP were recently investigated (10–12). The viscoelastic properties of statherin, PRPs, and mucins in the salivary pellicles reduce by 20-fold the mastication load (5, 13). Statherin also plays a role in the onset of periodontal diseases, which are marked by the adherence and colonization of various bacteria to supragingival and subgingival surfaces (14–16). Statherin and the PRPs mediate the adhesion of bacterial species to the tooth surface (17–22). These organisms preferentially adhere to immobilized statherin on HAP surfaces rather than to the free protein in solution (19, 22), leading to the hypothesis that surface adsorption exposes receptor sites in statherin to bacterial fimbrillin binding. Recent studies identified C-terminal residues L29–F43 and residues P33–Q39 in statherin as binding domains for *Porphyromonas gingivalis* and *Fusobacterium nucleatum* fimbriae, respectively (20, 22).

Earlier CD and NMR studies (23, 24) found that statherin is structurally disordered in aqueous solution. In 50% trifluoroethanol/water mixtures, statherin exhibits an α-helical structure at the N-terminal region (residues D1–Y16), a polyproline type II (P_{II}) helix in the intermediate region (residues G19–Q35), and a 3_{10} helix in the C terminus (residues P36–F43) (23). Polyproline helices are commonly found in the unfolded state of proteins and are now viewed as preorganized secondary motifs designed to accelerate the folding process (25). Previous solid-state NMR measurements of statherin adsorbed to HAP demonstrated that the N–terminal domain (residues D1–G12) is in an α-helical conformation (26). NMR relaxation measurements of the dynamics in this domain showed that the acidic N-terminal pentapeptide is immobilized, consistent with the previous observation that this region constitutes the HAP–binding footprint (26).

The ability to measure the molecular structure of biomolecules in heterogeneous systems with solid-state NMR in molecular details is unique to the technique (27). Secondary and tertiary structural constraints are obtained through selective isotopic labeling and accurate geometric measurements (28–30). The challenge in determining the 3D fold of statherin on HAP (and many other proteins) is that there is little or no direct structural information available to guide the design of isotopic labeling sites that would probe for globular structure. Here, we use the structure prediction algorithm ROSETTA (31) to generate an energy-minimized cluster of putative structures for statherin. A statistical analysis of interatomic distances and dihedral angles in this cluster provides an isotopic labeling scheme with high propensity for producing confirmatory results for the particular secondary and tertiary structural features sought. We report measurements of backbone torsion angles (residues P33–Y34) and carbonyl-amide distances (residues Y34–Y38) indicating that the C-terminal receptor site for bacterial adhesion adopts an α-helical conformation in statherin adsorbed to HAP crystals. We also measured long-range distances between carbonyl carbons in the C terminus (residues P33–Y34) and a fluorine atom (residue P23) showing that this motif closes back onto the protein's proline-rich region (residues Y16–P28) through a series of backbone turns. These results demonstrate the structure of the region in the protein that is recognized by pathogens and provide the overall fold of the protein when it binds to its natural solid substrate, HAP. They provide a structural context for better understanding of the *in situ* functions that this salivary protein performs.

Results

Modeling and Labeling Strategy. Recent improvements in computational structure prediction (32, 33) provide an interesting avenue for iteratively defining and refining 3D protein structures by choosing isotopic labeling sites and acquiring targeted structural NMR data. This strategy should in principle greatly reduce the data required to deduce the structure of proteins. Because no structural

Author contributions: G.G., P.S.S., and G.P.D. designed research; G.G. performed research; R.G. and O.S.-F. contributed new reagents/analytic tools; G.G., R.G., O.S.-F., D.B., and G.P.D. analyzed data; and G.G., P.S.S., and G.P.D. wrote the paper.

The authors declare no conflict of interest.

This article is a PNAS direct submission.

Abbreviations: HAP, hydroxyapatite; REDOR, rotational echo double resonance; CSA, chemical shift anisotropy.

[¶]Present address: Department of Molecular Genetics and Biotechnology, Hebrew University School of Medicine, Hadassah Medical School, Jerusalem 91120, Israel.

[‖]To whom correspondence may be addressed. E-mail: stayton@u.washington.edu or drobny@chem.washington.edu.

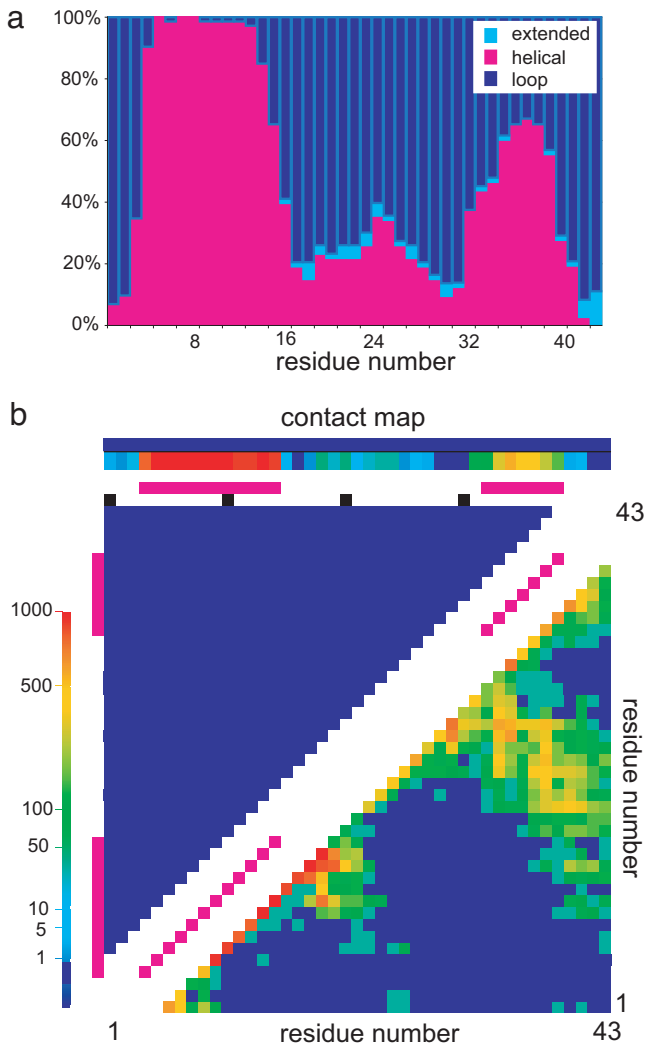

Fig. 1. Modeling statherin structure using the ROSETTA *ab initio* algorithm. (*a*) A histogram showing the percentage of the three basic secondary motifs along the backbone in the predicted 31-model cluster. (*b*) Contact map for the 31-model cluster. Diagonal squares, shown in pink, indicate short contacts between adjacent residues characteristic of an α-helix structure. Contacts that are shown as colorful squares perpendicular to the main diagonal in the lower right triangle indicate long-range contacts between residues far apart in the sequence. Common features between the models were used to select sites on the protein for incorporation of NMR labels.

homologues were available for the sequence of human statherin, the *ab initio* protocol of ROSETTA was used to generate structural models of the protein. Nearly all 1,000 models in the starting set predicted that the protein's N terminus (residues 3–15) is α-helical, as demonstrated experimentally (26). The models were then divided into subsets based on their structural similarity with the largest cluster comprised of 31 models. The histogram showing the percentage of either an extended, helix or loop backbone secondary structure, together with the contact map correlating residues by their spatial proximity, is depicted in Fig. 1. In both structural representations, a predicted α-helical segment at the C terminus of the protein (residues Q32–Q40) is seen. The intermediate segment has a higher structural dispersion with two turn regions at G19 and P31 that were common to some of the models seen in the contact map. Selection of an isotope labeling scheme for the protein sample was derived from analysis of the torsion angles and distances between pairs of atoms across the models and using only positions that are conserved in different species. Histograms of these structural parameters for the selected label positions are given in Fig. 2. Two consecutive carbonyl atoms on residues P33 and Y34 were ^{13}C-labeled and an amide on Y38 to extract the secondary structure in this region. Replacement of hydrogen with a fluorine atom on the 4′ position of P23 was used for long-range carbon–fluorine distance measurements between carbonyl carbon labels in the C terminus and the side chain of a proline near the protein center. The following labels, DpSpSEEKFLRRIGRFGYGY[**2-^{13}C**]GPYQ[**4′-^{19}F**]P23VPEQPLYPQ[**1-^{13}C**]P33[**1-^{13}C**]Y34QPQ[**^{15}N**]Y38QQYTF, were therefore incorporated in the synthesis of statherin. The phosphorylated serine residues in the sequence are denoted by pS.

Solid-State NMR Experiments. Rotational echo double resonance (REDOR) (34) experiments with 180° pulses alternating between the detect and dephase channels (35) (Fig. 6, which is published as supporting information on the PNAS web site) were used to obtain all distance and angle parameters in the CCN and CCF atom triads. For these label sets both homonuclear and heteronuclear dipolar parameters can be obtained by using the REDOR experiment (36). The reference measurement (S_0) in the version of the REDOR pulse sequence used in our experiments is similar to the simple excitation for the dephasing of rotational echo amplitudes measurement designed to extract the dipolar interaction between like-spins (37). It gives rise to a decaying signal arising from the ^{13}C–^{13}C dipolar interaction between the carbonyl labels recoupled by the pulses and the chemical shift anisotropy (CSA) difference tensor (Fig. 3*a*). Here, it was used to obtain the values for the (ϕ,ψ) torsion angles between the two labels relying on the known orientation of the carbonyl carbon CSA principle components relative to bond directions of that carbon in the peptide backbone (38). The resulting angles (Table 1) are consistent with a compact α-helical conformation of the backbone at this position (Fig. 3*c*). The CN-REDOR and the CF-REDOR measurements were carried out at different fields and different spinning rates as described in *Methods* for technical reasons only. The S_0 curves used to calculate the REDOR curves shown in Fig. 4 are somewhat different from the S_0 curve presented in Fig. 3 because they were carried out under different conditions (different field for the CCN measurement and different spinning rate for the CCF measurement). They were confirmed with simulations to give rise to similar torsion angle values as deduced from the curve shown in Fig. 3. The individual S_0 and S curves for the CCN measurement are shown in Fig. 7, which is published as supporting information on the PNAS web site. The CN-REDOR curve (S/S_0) gave rise to a [1-^{13}C]Y34-[^{15}N]Y38 distance of 4.0 Å (Fig. 4 *a* and *d*) that is indicative of a hydrogen bond stabilizing the α-helical structure. The angle between the [1-^{13}C]Y34-[^{15}N]Y38 and the [1-^{13}C]P33-[^{13}C]Y34 vectors was 95(±5)°, implying that the hydrogen bond is nearly parallel to the helix axis (Fig. 4*c*). The CF-REDOR curve (S/S_0) shown in Fig. 4*e* demonstrates that the C terminus labels are in proximity to the fluorine label, constraining the distance of these labels from the [4′-^{19}F]P23 label to 8.8 and 10.3 Å (Fig. 4 *g* and *h*). The two labeled carbonyl carbons are unresolved in the ^{13}C NMR spectra (Fig. 8, which is published as supporting information on the PNAS web site), and thus the assignment of the closer carbon atom cannot be determined. A summary of all distance and orientation parameters derived from the NMR measurements is given in Table 1. All errors reported in Table 1 are based on a $1^{*}\sigma$ confidence in the χ^2 plots shown in Figs. 3 and 4.

Refinement of the statherin structure was done by constraining the original 1,000-model set with the geometric measurements. The resultant eight structures, aligned along the backbone atoms in the two helices, are given in Fig. 5. They exhibit an average pair rmsd of 2.5 Å with higher structural dispersion in the intermediate region where constraints have not yet been

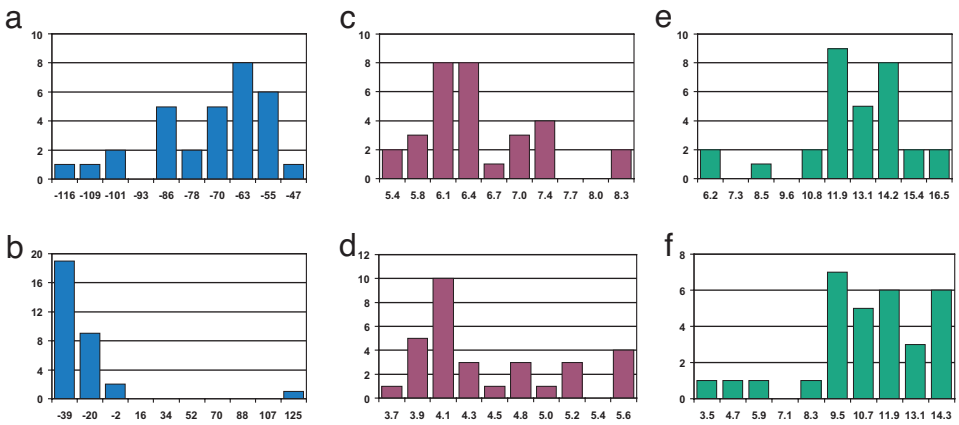

Fig. 2. Histograms showing the distribution of torsion angles and distances between labels across the 31-model cluster. (*a* and *b*) Φ angle (*a*) and Ψ angle (*b*) values for the backbone torsion angles between the two carbonyl labels [1-^{13}C]P33 and [1-^{13}C]Y34. (*c* and *d*) Nitrogen–carbon distances between the [^{15}N]Y38 label and the [1-^{13}C]P33 label (*c*) and the [1-^{13}C]Y34 label (*d*) (in angstroms). (*e* and *f*) Fluorine–carbon distances between the [4′-^{19}F]P23 label and the [1-^{13}C]Y33 label (*e*) and the [1-^{13}C]Y34 label (*f*) (in angstroms).

measured. The small folded core is created by the folding of the C-terminus helical region (residues P33–Y38) back onto the intermediate region through a loop region defined by proline residues. The C-terminus helix can be tilted at different angles with respect to the N-terminal helix because of the limited number of constraints between the two regions. The resultant torsion angle and distance values are not 1:1 correlated with maxima in the calculated values in the histograms (e.g., ϕ angle). Only a single model of the eight is common to the 31-model cluster used for labeling selection, underscoring the predisposition that the predicted structure serves as a guideline for selection of label sites. The ROSETTA program thus successfully narrowed the search for structural elements in the folded protein and then enabled a construction of the protein fold based on the experimental distance constraints. The oscillatory shape of the experimental curve given in Fig. 3*a* at long mixing times implies that the distribution of angles around the measured P33-Y34 torsion angles is quite narrow. For the CN and CF distance measurements, data points are not available at the oscillatory region of the curve, and therefore it is harder to assess how broadly distributed the distances between different protein molecules are. However, for very broad distributions, the shape of the earlier part of the dephasing curves will be different from the one observed (39).

Discussion

Proteins commonly undergo large conformational changes upon adsorption to solid surfaces (40, 41). This transition can substantially affect their biological activity (42), particularly in proteins that evolved to interact with surfaces as substrates. While proteins predominantly undergo unfolding upon adsorption to surfaces (41, 43), statherin exhibits adsorption associated folding that is related to its particular functions both off and on the surface. This significant structural transition is coupled to the key functions that statherin exhibits, including the binding of early crystal nuclei to suppress the onset of calcium phosphate crystallization and adsorption onto nucleated crystals to inhibit their growth (5, 44). We have previously proposed that statherin retains an unfolded structure in solution to circumvent the orientation of negatively charged residues in a defined geometry that would stabilize calcium phosphate crystal nucleation (45). The folding of statherin into a globular conformation may be important for secondary growth inhibition function on the crystal surface. The compact fold of statherin guarantees efficient coverage of the crystal faces and effective masking of charged residues that may otherwise promote formation of new crystal layers. This is a new extension of activity-coupled folding of proteins (46) to biomineralization where some proteins are found to be unstructured in aqueous solution (47, 48) and where the substrate is a solid inorganic surface.

Although the ROSETTA algorithm is used here as a modeling tool for label placement and in defining the set of structures that are constrained by the NMR measurement, the models derived from the calculations do not take into account the influence of the surface potential on the structure of the protein and therefore imply a plausible representation of the adsorbed protein structure. Interestingly, the ROSETTA predictions produced a large dispersion in the modeled structure and only less stringent similarity demand produced the cluster used, which by itself points to a less defined conformation as observed in solution. An accurate modeling of the structure of statherin on HAP should include the effects that surface energetics might impose on the protein fold.

These results have additional biological implications. Statherin mediates the binding of several bacterial fimbriae via its C-terminal region only when it is adsorbed onto HAP. Previous work has suggested that this recognition site is being exposed during the adsorption of statherin to the mineral surface (49). The α-helical conformation in the bacterial recognition site (residues L29–F43), shown here to form upon adsorption, provides a clear avenue for the differential recognition of immobilized vs. free statherin by bacteria. NMR measurements in 50% trifluoroethanol solution report a 3_{10} helix in a C-terminal region (23) that slightly overlaps with the region where the solid-state NMR measurements were taken. The possibility of a 3_{10} helix existing between residues 34 and 38 in the adsorbed protein's C terminus is ruled out because the CN-REDOR measurements are designed to distinguish between the two secondary motifs (50).

The C terminus of statherin has been previously shown to be key to the lubricative action of statherin on tooth enamel (5), and the connection between helical secondary structure and viscoelastic function has been made with human serum albumin (51). The folding of statherin's C terminus into an α-helical conformation thus serves as a structural context for understanding both fimbrillin binding and consequently bacterial adhesion, and the important lubricative properties of bound statherin. The lubricative action of statherin in concert with other proteins in the pellicle should be greatly influenced by the structure the protein assumes when adsorbed. Particularly, if a cooperative

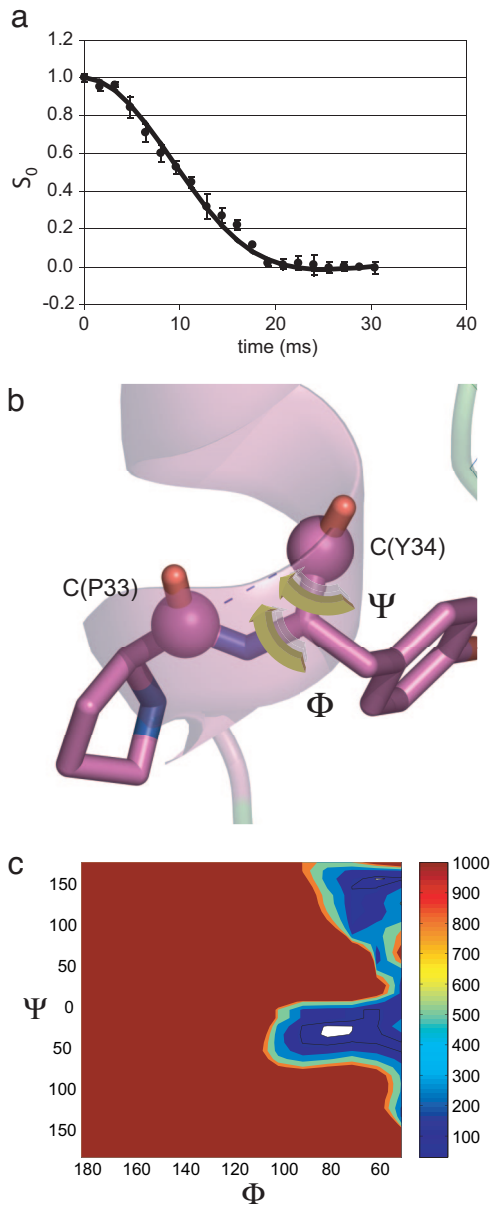

Fig. 3. ^{13}C simple excitation for the dephasing of rotational echo amplitudes (SEDRA) NMR decay curve showing the carbon signal intensity as a function of the length of time the pulses are applied. (*a*) ^{13}C signal decay in the REDOR reference (S_0) experiment (normalized to the intensity of the first data point) showing dephasing behavior caused by recoupling of the ^{13}C-^{13}C dipolar interaction. The fit to this decay curve is used to extract the structural parameters. (*b*) Structural parameters that influence the decay curve. Graphic visualization of the relation between the relative orientation of CSA tensors (green) and the Φ and Ψ angles in the two carbonyl labels. (*c*) χ^2 analysis of data based on simulations using the torsion angle dependence. A contour plot of the $\chi^2(\Phi,\Psi)$ function showing angular values in the SEDRA data are best fit. Confidence level of $1*\sigma$ is shown as the lowest contour (white).

mechanism of friction reduction exists, recognition between different proteins requires that statherin adopts a well determined structure in the pellicle (3).

Methods

Protein Synthesis and Adsorption. Amino acids with ^{19}F isotope were purchased from Bachem (King of Prussia, PA), and amino acids with [99%-^{13}C] and [98%-^{15}N] isotopes were purchased from Cambridge Isotope Laboratories (Cambridge, MA) and

Table 1. Summary of measured structural parameters in adsorbed statherin

Statherin	Distance, Å	Torsion angles, Ψ, Φ	Polar angles, θ_D, Φ_D
[1-^{13}C]P33-[1-^{13}C]Y34	3.12 (±0.13)	−40° (±10), −75° (±15)	
[1-^{13}C]P33-[^{15}N]Y38	5.3 (±0.5)		100° (±4), 300° (±10)
[1-^{13}C]Y34-[^{15}N]Y38	4.0 (±0.5)		88° (±5), 273° (±13)
[1-^{13}C](P33 or Y34)-[^{19}F]P23	8.8 (±0.8)		95° (±15), 294° (±30)
[1-^{13}C](P33 or Y34)-[^{19}F]P23	10.5 (±1.0)		90° (±15), 282° (±35)

Polar angles are given in the principle axes system of [1-^{13}C]P33 CSA tensor. Errors reported are based on one standard deviation in the χ^2 analysis of the data. Construction of the χ^2 function took experimental errors into account.

incorporated by using solid-phase peptide synthesis based on Fmoc chemistry. The protein was purified and analyzed as described (10). The protein was prepared in a phosphate buffer (100 mM NaCl/40 mM KCl/4.3 mM Na_2HPO_4/1.4 mM KH_2PO_4, pH 7.4) to maintain constant pH conditions at temperatures below the freezing point of water. A total of 16 mg of protein was adsorbed by mixing 30 mg of the protein in phosphate buffer with 100 mg of HAP in the same phosphate buffer for 4 h. After centrifugation, the wet pellet containing the complex was washed three times with the phosphate buffer. The last wash contained only traces of protein in the buffer. The mineral–protein complex was then flash-frozen with liquid nitrogen before insertion into a precooled NMR probe to increase cross-polarization efficiency while avoiding water crystallization or salt depletion. From previous studies in the group, no substantial changes in the secondary structure of the protein's N terminus were observed before upon freezing the protein–mineral complex (26). In another work, statherin showed no structural changes at temperatures above ambient (24). Any structure change accompanying freezing should be carefully examined by conducting a temperature-dependent structural study.

NMR Experiments. ^{13}C-^{13}C reference and ^{13}C-^{19}F REDOR measurements were carried out on a home-built wide-bore 500-MHz spectrometer by using a Varian (Palo Alto, CA) 4-mm ^{1}H-^{19}F-^{13}C triple-tuned probe. The ^{13}C-^{13}C measurement was carried out at a spinning rate of 5 kHz, and the ^{13}C-^{19}F REDOR measurement (S_0 and S) was carried out at a spinning rate of 8 kHz to achieve better signal-to-noise ratios. Carbon cross-polarization was achieved by using a ramped field between 46 and 23 kHz on the protons and a field of 35 kHz on the carbon with a contact time of 2 ms. Carbon 180° pulses and fluorine 180° pulses at respective fields of 45 and 62 kHz were used. Continuous wave decoupling at a field of 85 kHz was used during the whole experiment. ^{13}C-^{15}N REDOR measurements were carried out on a DSX300 spectrometer (Bruker, Billerica, MA) with a 4-mm ^{1}H-^{13}C-^{15}N triple-tuned probe. Carbon cross-polarization was achieved by using a ramped field between 55 and 27 kHz on the protons and a field of 40 kHz on the carbon with a contact time of 2 ms. Carbon 180° pulses and nitrogen 180° pulses at respective fields of 56 and 30 kHz were used. Proton decoupling at a field of 75 kHz using the two pulse phase modulation sequence was used to decouple the protons through the experiments. CN-REDOR experiments were carried out at a spinning rate of 5 kHz. All experiments were carried out at −50°C. Cooled nitrogen gas

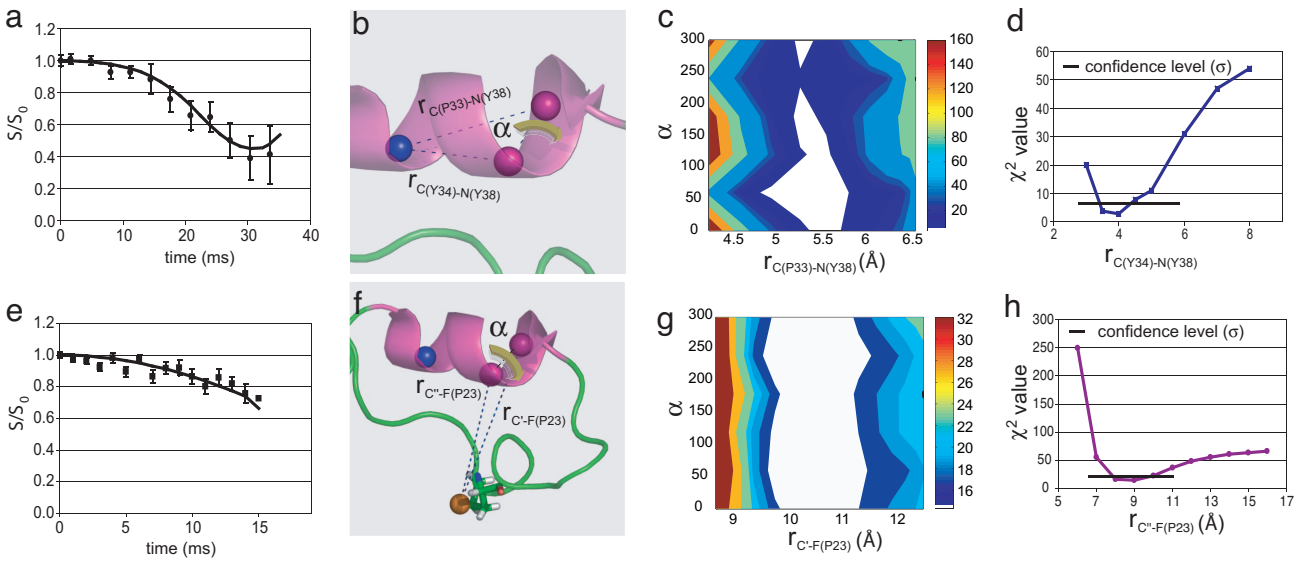

Fig. 4. ^{13}C-^{15}N and ^{13}C-^{19}F REDOR decay (S/S_0) curves showing the carbon signal intensity as a function of the length of time the pulses are applied. (*a*) ^{13}C signal decay (S/S_0) from recoupling of the ^{13}C-^{15}N dipolar couplings in a REDOR experiment. (*b*) Dipolar interaction parameters in the C(P33)-C(Y34)-N(Y38) spin triad. (*c*) The contour plot of the $\chi^2(r_{C(P33)\text{-}N(Y38)},\alpha)$ function. (*d*) The graph of the $\chi^2(r_{C(Y34)\text{-}N(Y38)})$ function showing values for which the CN-REDOR data are minimized. (*e*) ^{13}C signal decay (S/S_0) from recoupling of the ^{13}C-^{19}F dipolar couplings in a REDOR experiment. The fits to these decay curves are used to extract the structural parameters. Shown are graphic visualizations of the structural parameters that influence the decays and χ^2 analysis of simulation and data based on these parameters. The parameter α represents rotation of the heteronuclear dipolar vectors around the CC vector. (*f*) Dipolar coupling parameters in the C(P33)-C(Y34)-F(P23) spin triad. Here, we denote the two carbons as C′ and C″ because they are indistinguishable in the ^{13}C spectrum. (*g* and *h*) The contour plot of the $\chi^2(r_{C'\text{-}F(P23)},\alpha)$ function (*g*) and the graph of the $\chi^2(r_{C'\text{-}F(P23)})$ function (*h*) demonstrate values for which the CF-REDOR data are fit by simulations. Confidence level of $1*\sigma$ is shown as the lowest contour (white).

flow was used for sample spinning at 5 kHz and to achieve low temperatures at the sample. Dried and cooled air was used to cool the sample spun at 8 kHz on the 500-MHz spectrometer. Reference and dephasing REDOR experiments all were carried out by using XY8 phase cycling to correct for inhomogenous radio frequency fields and other pulse imperfections.

Spin Dynamics Simulations. Calculations were carried out by using the SIMPSON (52) spin dynamics program. For spin-pair simulations all CSA and dipolar interaction parameters were taken into account. CSA parameters were computed from analysis of sideband patterns in cross-polization magic angle spinning experiments and were confirmed against values from the literature (53). Known directions of the CSA tensor components relative to the bonding of the carbonyl carbon in the backbone frame (38) were used to generate all possible carbonyl-carbonyl relative CSA orientations (Euler angles) based on rotations around the torsion angles (ϕ, ψ) for the $\phi <$ 0 section in the Ramachandran plot. For spin-triad simulations all interaction parameters of the ^{13}C spins and all dipolar interaction parameters of the heteronuclear dipolar interactions were taken into account. The geometry of the heteronuclear dipolar interactions was computed relative to the [1-^{13}C]P33 CSA principle axes system by placing the heteroatom at variable distances from the two carbon atoms and rotating the dipolar vectors around the C-C vector to cover all conformational space. $^{13}C_2$-X (X = F or N) simulations used all premeasured ^{13}C-^{13}C CSA and dipolar parameters.

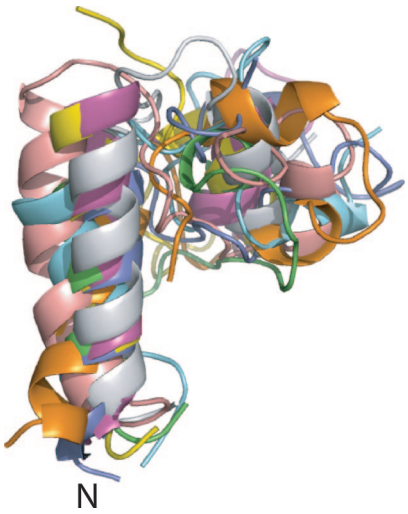

Fig. 5. Superposition of the eight models that agree with the constraints derived from the solid-state NMR measurements. These models are derived from the full set of 1,000 models. Alignment of the models was based on rmsd calculation of segments (residues D1–G15) and (residues P33–Y38) between the eight models.

Data Analysis. ^{13}C-^{13}C simulations with ($\phi(r_{C\text{-}C}),\psi$) as variables were used to create a grid of expected dephasing curves for allowed backbone conformations in the Ramachandran plot ($\phi < 0$). Calculated $\chi^2(\phi, \psi)$ function was used to fit experimental data. $^{13}C_2$-X (X = F or N) simulations with the two heteronuclear distance vectors and their orientation in the principal axes system of the [^{13}C]P33 CSA as variables (Fig. 4) were used to create an array of expected REDOR curves. These simulations used all measured ^{13}C-^{13}C CSA and dipolar parameters. The $\chi^2(r_{C33\text{-}N}, r_{C34\text{-}N}, \alpha)$ and $\chi^2(r_{C'\text{-}F}, r_{C''\text{-}F}, \alpha)$ functions were then calculated. Minima in the χ^2 function are separated into $\chi^2(r_{C33\text{-}N})$ or $\chi^2(r_{C'\text{-}F})$ projections depicted in Fig. 4 *d* and *h*, respectively and 2D slices of $\chi^2(r_{C34\text{-}N}, \alpha)$ or $\chi^2(r_{C''\text{-}F}, \alpha)$, taken at those minima, in the contour plots shown in Fig. 4 *c* and *g*.

Protein Structure Prediction. A set of 1,000 structural models were created by the ROSETTA *ab initio* structure prediction pro-

tocol starting from extended chains, as described (31). Local structural preferences were modeled based on a fragment library that represents the range of accessible local structures for short segments of the protein chain in a database of known protein structures. Compact structures were assembled by randomly combining these fragments, using a Monte Carlo simulated annealing search. An initial step using nonamer fragments was followed by a subsequent optimization with trimer fragments and final local backbone optimization. Non-local interactions were evaluated with a scoring function derived from conformational statistics of known protein structures. These calculations did not take into account the surface potential energy of HAP or any solvent effects.

We thank Prof. Shimon Vega, Dr. Shifra Kababya, and Mrs. Tal Amitay for help with the REDOR experiment carried out at The Weizmann Institute of Science, Rehovot, Israel. This work was supported by National Dental Institute Grant DE-12554.

1. Schupbach P, Oppenheim FG, Lendenmann U, Lamkin MS, Yao Y, Guggenheim B (2001) *Eur J Oral Sci* 109:60–68.
2. Li J, Helmerhorst EJ, Yao Y, Nunn ME, Troxler RF, Oppenheim FG (2004) *Arch Oral Biol* 49:379–385.
3. Vitkov L, Hannig M, Nekrashevych Y, Krautgartner WD (2004) *Eur J Oral Sci* 112:320–325.
4. Yin A, Margolis HC, Yao Y, Grogan J, Oppenheim FG (2006) *Arch Oral Biol* 51:102–110.
5. Douglas, WH, Reeh ES, Ramasubbu N, Raj PA, Bhandary KK, Levine MJ (1991) *Biochem Biophys Res Commun* 180:91–97.
6. Proctor GB, Hamdan S, Carpenter SH, Wilde P (2005) *Biochem J* 389:111–116.
7. Hay DI, Moreno EC (1989) in *Human Saliva: Clinical Chemistry and Microbiology*, ed Tenovuo JO (CRC, Boca Raton, FL), Vol I, pp 131–150.
8. Johnsson M, Levine MJ, Nancollas GH (1993) *Crit Rev Oral Biol Med* 4:371–378.
9. Moreno EC, Kresak M, Hay DI (1978) *Arch Oral Biol* 23:525–533.
10. Goobes R, Goobes G, Campbell CT, Stayton PS (2006) *Biochemistry* 45:5576–5586.
11. Gibson JM, Raghunathan V, Popham JM, Stayton PS, Drobny GP (2005) *J Am Chem Soc* 127:9350–9351.
12. Raghunathan V, Gibson JM, Goobes G, Popham JM, Louie AE, Stayton PS, Drobny GP (2006) *J Phys Chem B* 110:9324–9332.
13. Hahn Berg IC, Lindh L, Arnebrant T (2004) *Biofouling* 20:65–70.
14. Lamont RJ, Jenkinson HF (1998) *Microbiol Mol Biol Rev* 62:1244–1263.
15. Dodds MWJ, Johnson DA, Yeh C-K (2005) *J Dent* 33:223–233.
16. Rudney JD, Chen R (2004) *Arch Oral Biol* 49:523–527.
17. Gibbons RJ, Hay DI (1988) *Infect Immun* 56:439–445.
18. Gibbons RJ, Hay DI, Schlesinger DH (1991) *Infect Immun* 59:2948–2954.
19. Xie H, Gibbons R, Hay D (1991) *Oral Microbiol Immun* 6:257–263.
20. Amano A, Kataoka K, Raj PA, Genco RJ, Shizukuishi S (1996) *Infect Immun* 64:4249–4254.
21. Nagata H, Sharma A, Sojar HT, Amano A, Levine MJ, Genco RJ (1997) *Infect Immun* 65:422–427.
22. Sekine S, Kataoka K, Tanaka M, Nagata H, Kawakami T, Akaji K, Aimoto S, Shizukuishi S (2004) *Microbiology* 150:2373–2379.
23. Naganagowda GA, Gururaja TL, Levine MJ (1998) *J Biomol Struct Dyn* 16:91–107.
24. Elgavish GA, Hay DI, Schlesinger DH (1984) *Int J Peptide Protein Res* 23:230–234.
25. Kentsis A, Mezei M, Osman R (2005) *Proteins Struct Funct Bioinf* 61:769–776.
26. Long JR, Shaw WJ, Drobny GP, Stayton PS (2001) *Biochemistry* 40:15451–15455.
27. Thompson LK (2002) *Curr Opin Struct Biol* 12:661–669.
28. Cegelski L, Kim SJ, Hing AW, Studelska DR, O'Connor RD, Mehta AK, Schaefer J (2002) *Biochemistry* 41:13053–13058.
29. Tycko R (2003) *Biochemistry* 42:3151–3159.
30. Drobny GP, Long JR, Karlsson, T, Shaw W, Popham J, Oyler N, Bower P, Stringer J, Gregory D, Mehta M, *et al.* (2003) *Annu Rev Phys Chem* 54:531–571.
31. Rohl CA, Strauss CEM, Misura KMS, Baker D (2004) *Methods Enzymol* 383:66–93.
32. Schueller-Furman O, Wang C, Bradley P, Misura K, Baker D (2005) *Science* 310:638–642.
33. Bradley P, Misura KMS, Baker D (2005) *Science* 309:1868–1871.
34. Gullion T, Schaefer J (1989) *Adv Magn Reson* 13:57–83.
35. Gullion T, Garbow J (1991) *J Magn Reson* 95:442–445.
36. Goobes G, Raghunathan V, Louie EA, Gibson JM, Olsen GL, Droby GP (2006) *Solid State Nucl Magn Reson* 29:242–250.
37. Gullion T, Vega S (1992) *Chem Phys Lett* 194:423–428.
38. Tycko R, Weliky DP, Berger AE (1996) *J Chem Phys* 105:7915–7930.
39. Mueller KT, Jarvie TP, Aurentz DJ, Roberts BW (1995) *Chem Phys Lett* 242:535–542.
40. Norde W (1986) *Adv Colloid Interface Sci* 25:267–340.
41. Haynes CA, Norde W (1995) *J Colloid Interface Sci* 169:313–328.
42. Agashe M, Raut V, Stuart SJ, Latour RA (2005) *Langmuir* 21:1103–1117.
43. Andrade JD, Hlady V (1986) *Adv Polym Sci* 79:1–63.
44. Hay DI, Smith DJ, Schluckebier SK, Moreno EC (1984) *J Dent Res* 63:857–863.
45. Stayton PS, Drobny GP, Shaw WJ, Long JR, Gilbert M (2003) *Crit Rev Oral Biol Med* 14:370–376.
46. James LC, Tawfik DS (2003) *Trends Biochem Sci* 28:361–368.
47. Tompa P (2003) *BioEssays* 25:847–855.
48. Dyson HJ, Wright PE (2005) *Nat Rev Mol Cell Biol* 6:197–208.
49. Amano A, Nakamura T, Kimura S, Morisaki I, Nakagawa I, Kawabata S, Hamada S (1999) *Infect Immun* 67:2399–2405.
50. Marshall GR, Beusen DD, Kociolek K, Redlinski AS, Leplawy MT, Pan Y, Schaefer J (1990) *J Am Chem Soc* 112:963–964.
51. Heuberger MP, Widmer MR, Zobeley E, Glockshuber R, Spencer ND (2005) *Biomaterials* 26:1165–1173.
52. Bak M, Rasmussen JT, Nielsen NC (2000) *J Magn Reson* 147:296–330.
53. Ye CH, Fu RQ, Hu JZ, Hou L, Ding SW (1993) *Magn Reson Chem* 31:699–704.